Supporting Information

Order-Disorder Transition-induced Band Nestification in $AgBiSe_2$-$CuBiSe_2$ Solid Solutions for Superior Thermoelectric Performance

Hanhwi Jang[a], Stanley Abbey[b], Woo Hyun Nam[c], Brakowaa Frimpong[b], Chien Viet Nguyen[d], Sung-Jae Joo[e], Ho Sun Shin[d], Jae Yong Song[d], Eugene N. Cho[f], Moohyun Kim[a], Yeon Sik Jung[a], and Min-Wook Oh[b]**

[a] Department of Materials Science and Engineering, Korea Advanced Institute of Science and Technology (KAIST), 291 Daehak-ro, Yuseong-gu, Daejeon, 34141, Republic of Korea

[b] Department of Materials Science and Engineering, Hanbat National University, 125 Dongseodae-ro, Yuseong-gu, Daejeon, 34158

[c] Energy Efficiency Materials Center, Korea Institute of Ceramic Engineering and Technology (KICET), Jinju, 52851, Republic of Korea

[d] Korea Research Institute of Standards and Science (KRISS), Daejeon, 34113, Republic of Korea

[e] Energy Conversion Research Center, Korea Electrotechnology Research Institute (KERI), Changwon, 51543, Republic of Korea

[f] KAIST Institute for NanoCentury, Korea Advanced Institute of Science and Technology (KAIST), 291 Daehak-ro, Yuseong-gu, Daejeon 34141, Republic of Korea

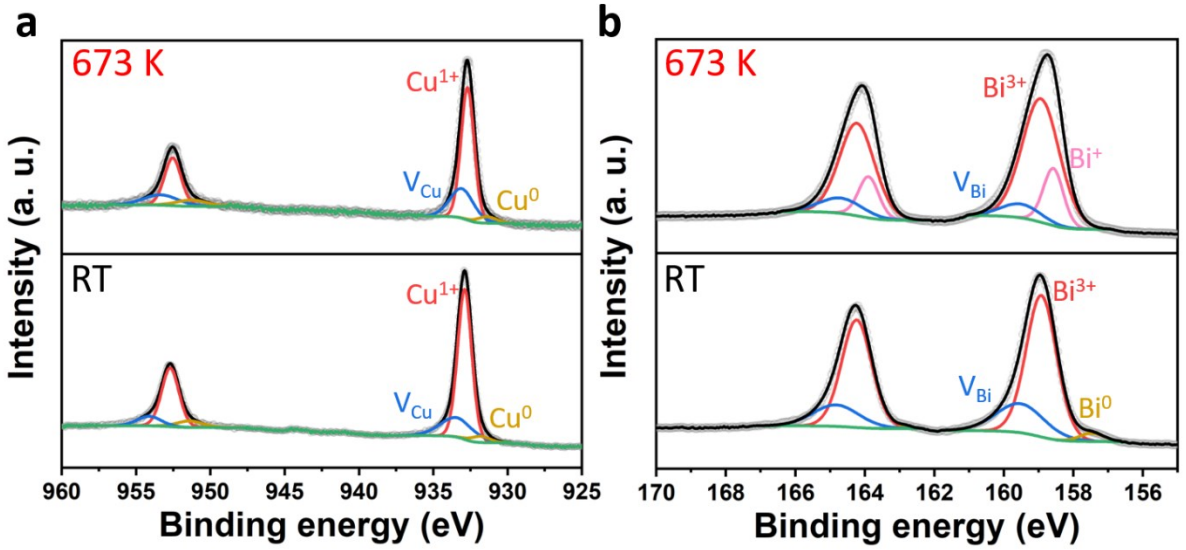

Figure S1. In-situ XPS spectrum of (a) Cu 3d scan and (b) Bi 4f scan of CABS-27 at room temperature and 673 K. It was found that most of the Cu consists of Cu with the 1+ valence state, which does not change significantly after a phase transition, meaning that Cu is incorporated into the Ag sites. On the other hand, the XPS spectrum of Bi reveals the existence of both Bi^0 and Bi^{3+}at room temperature.

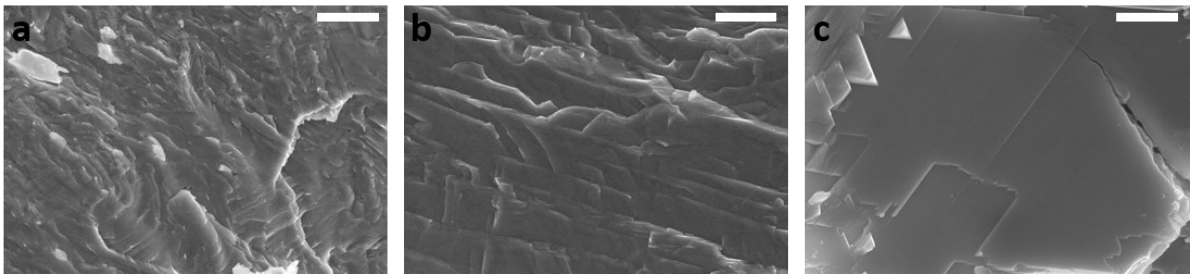

Figure S2. Representative SEM image of the fracture surface of (a) CABS-13, (b) CABS-20, and (c) CABS-27. Gradual increase of the average grain size is observed. Scale bar = 2 μm.

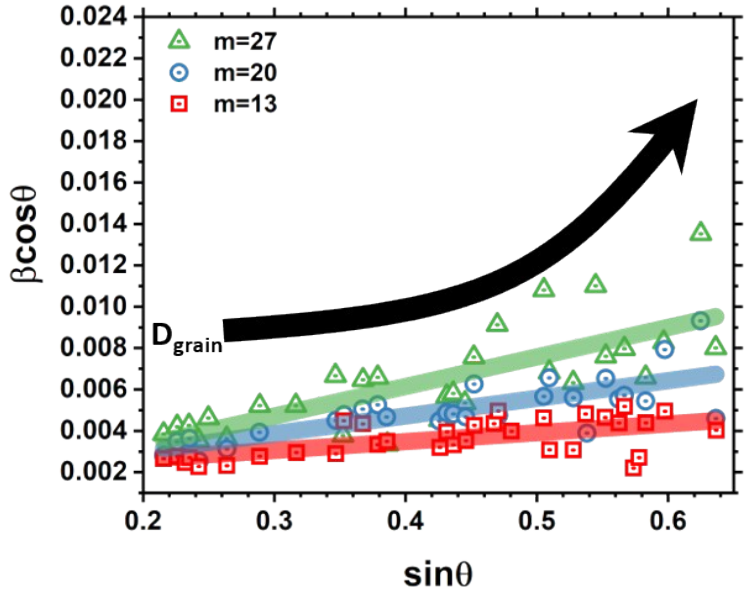

Figure S3. Williamson-Hall plot of CABS alloys showing an increase of the average crystallite size by Cu concentration.

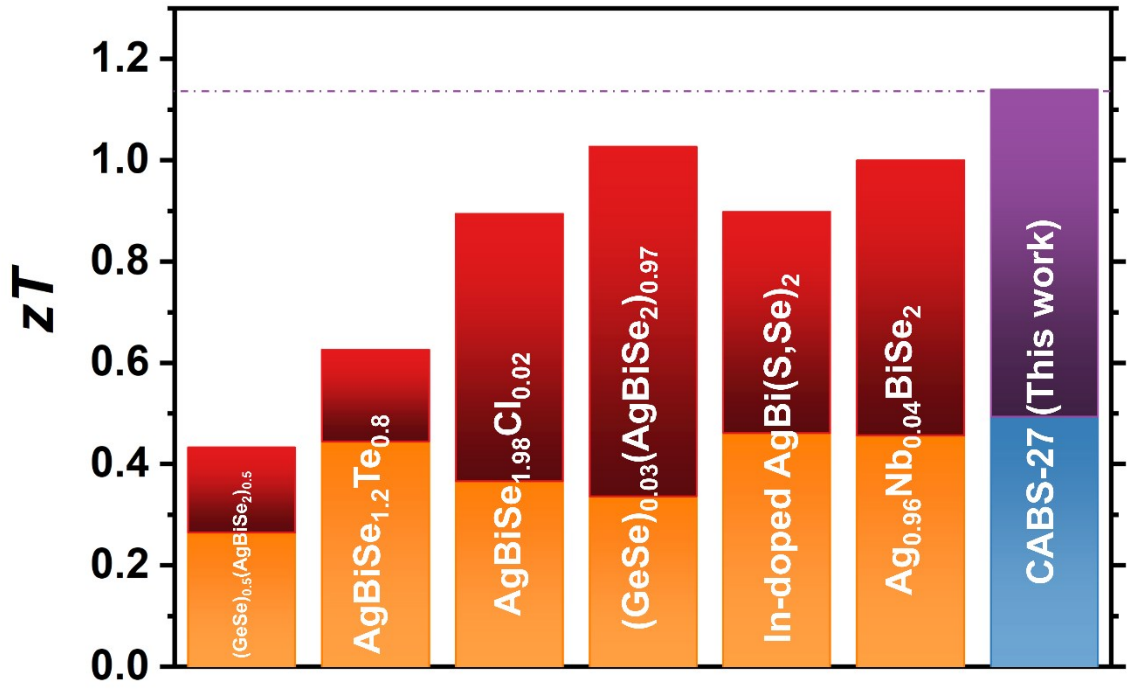

Figure S4. Comparison of TE properties among reported $AgBiSe_2$-based materials and CABS-27. Upper and lower panel denotes zT_{max} and zT_{avg}, respectively.

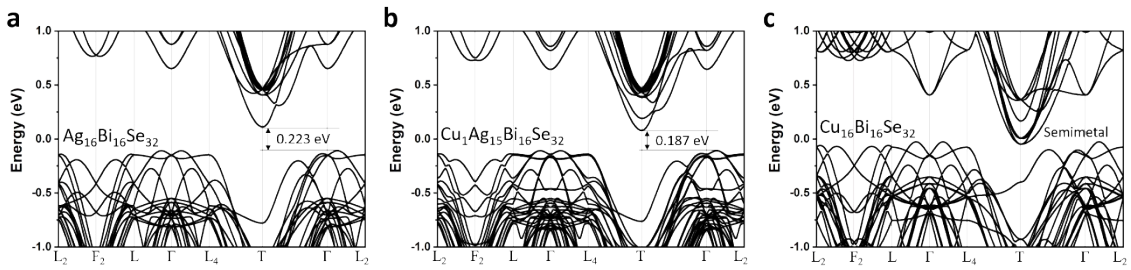

Figure S5. Calculated electronic band structure of ABS, CABS, and CBS with the $L1_1$ structure. Spin-orbit interaction was not considered in this calculation.

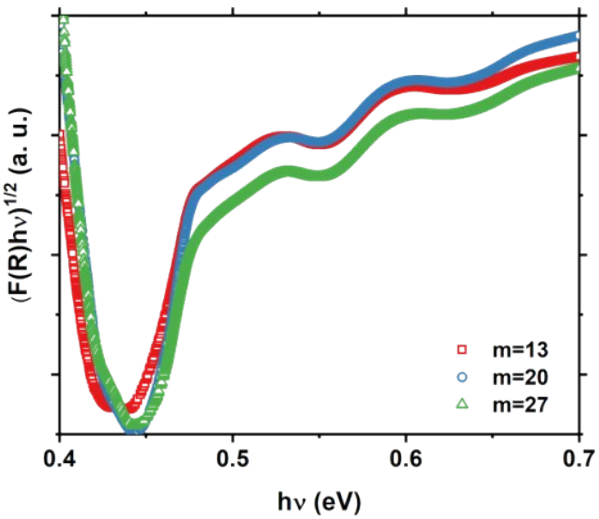

Figure S6. Optical absorption spectrum of CABS alloys at room temperature. No significant change of band gap is observed upon Cu alloying.

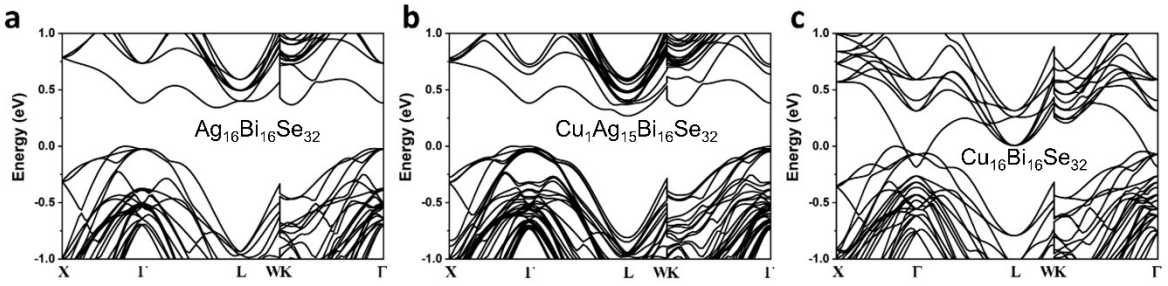

Figure S7. Calculated electronic band structure of ABS, CABS, and CBS with the *D*4 structure. Spin-orbit interaction was considered in this calculation.

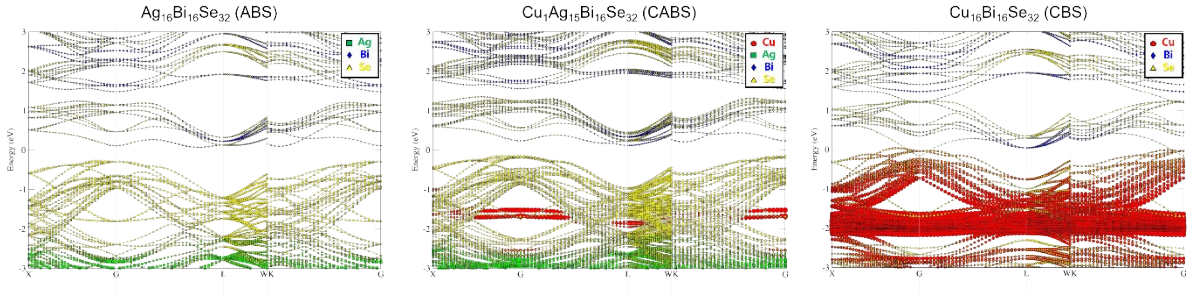

Figure S8. Atomic contribution of electronic band in $Ag_{16}Bi_{16}Se_{32}$ (ABS), $Cu_1Ag_{15}Bi_{16}Se_{32}$ (CABS), and $Cu_{16}Bi_{16}Se_{32}$ (CBS) with the *D*4 structure.

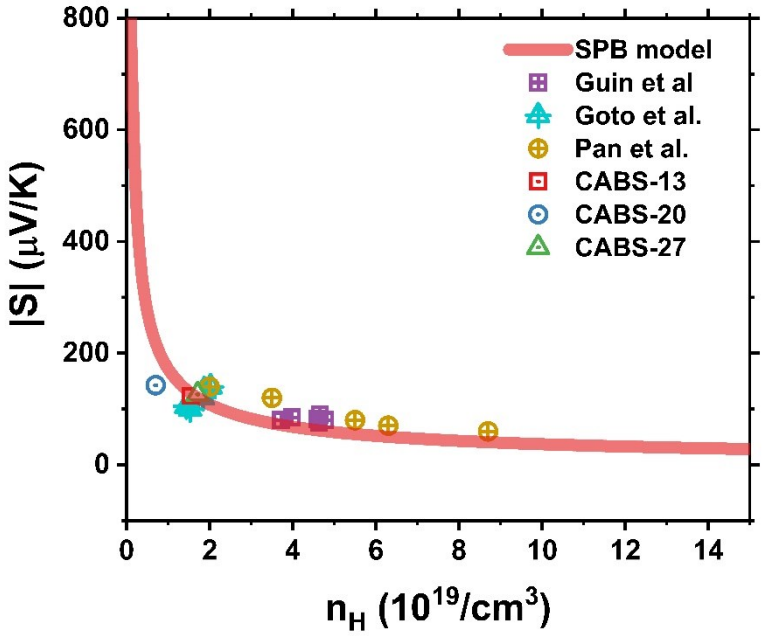

Figure S9. Pisarenko plot of CABS alloys and reported $AgBiSe_2$-based materials at room temperature. The theoretical Seebeck coefficient expected from the SPB model well describes the behavior of $AgBiSe_2$, meaning that the electronic structure is not changed significantly with Cu alloying in hexagonal crystal structure.

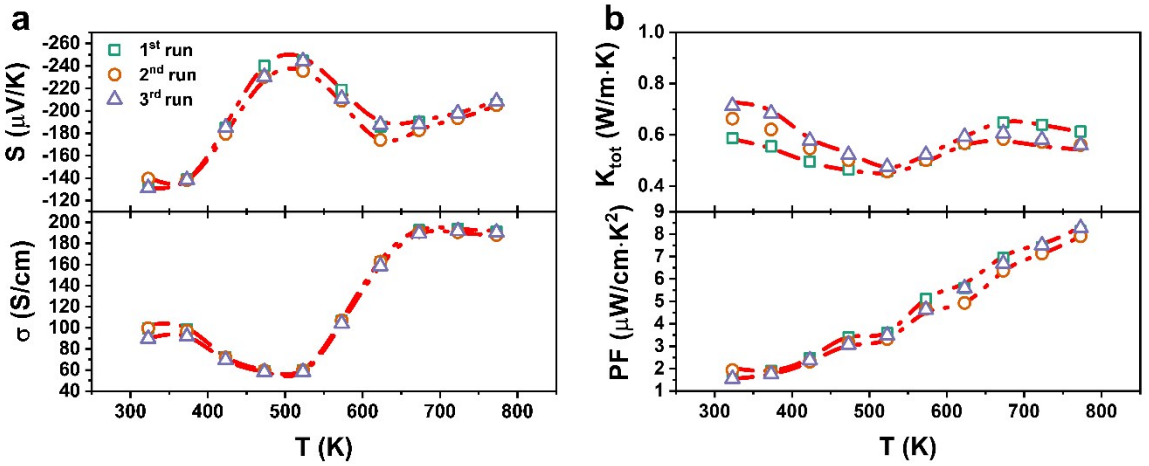

Figure S10. Temperature-dependent (a)Seebeck coefficient, electrical conductivity, (b) total thermal conductivity, and power factor of CABS-27 during three heating cycles. Dashed lines mean 95% confidence level of the measured values. Same symbol denotes same measurement trial.

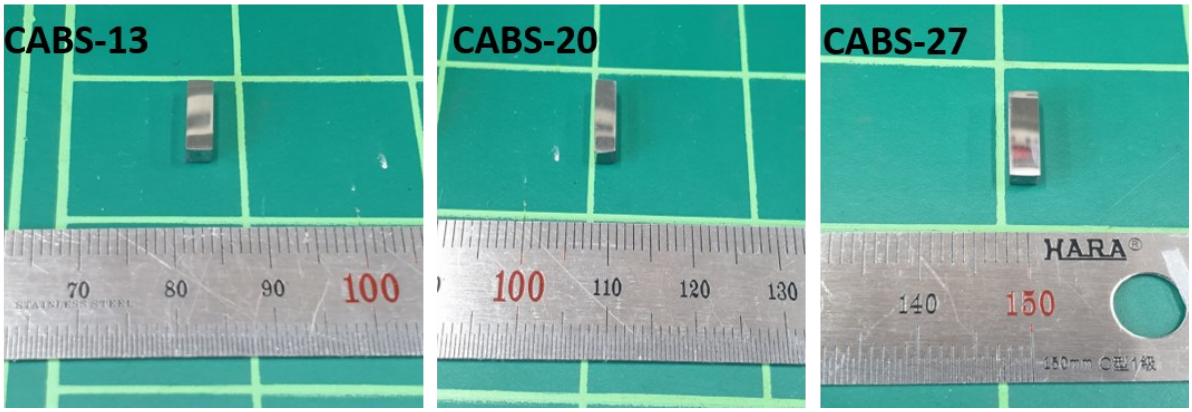

Figure S11. Digital photographs of high-quality polycrystalline CABS samples after TE property measurement. Neither significant mechanical deformation nor local melting were observed.

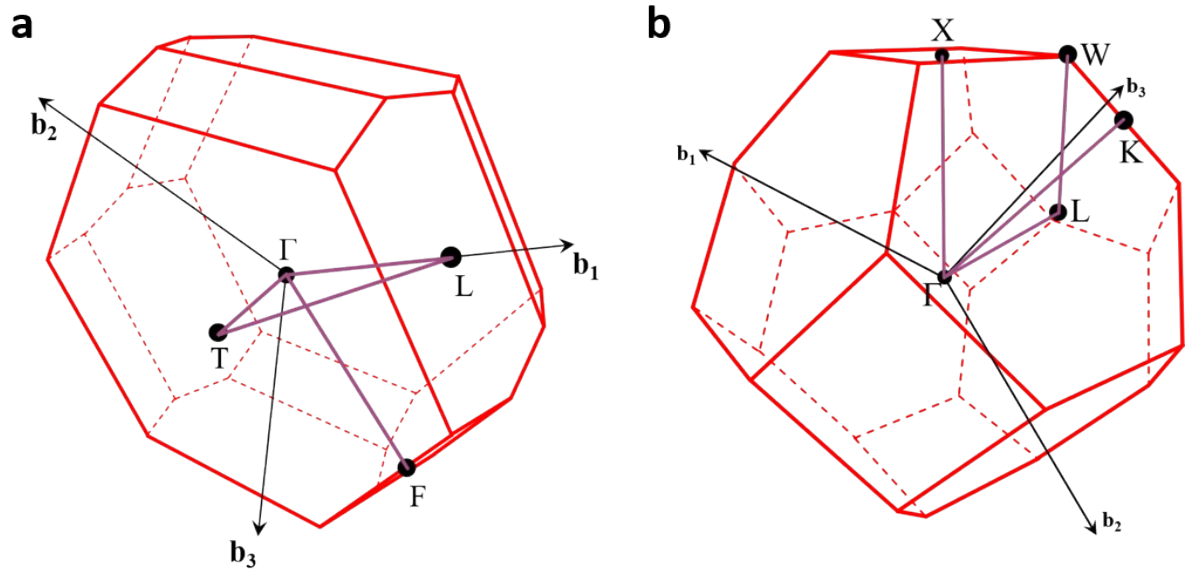

Figure S12. Brillouin zone and high symmetry k-points of (a) $L1_1$ structure and (b) $D4$ structure. Reciprocal cell vectors are denoted as b_1, b_2, and b_3, and k point paths for the calculation of the band structure are shown as purple line.

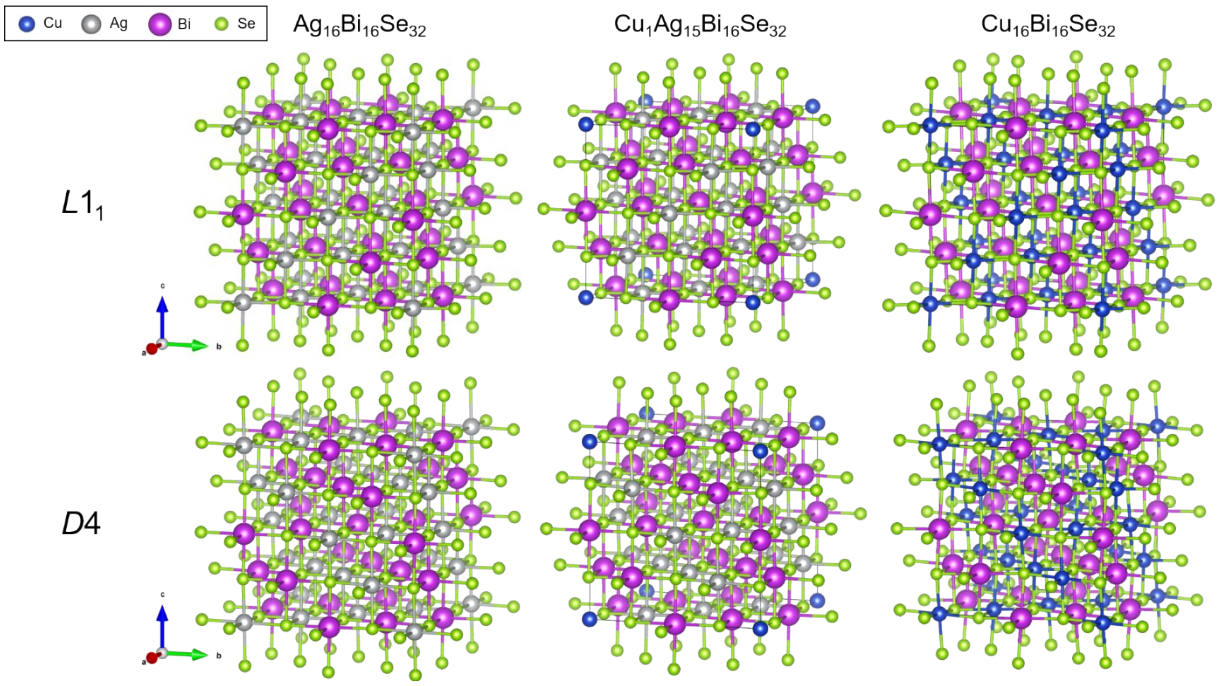

Figure S13. Fully optimized crystal structure of $Ag_{16}Bi_{16}Se_{32}$ (ABS), $Cu_1Ag_{15}Bi_{16}Se_{32}$ (CABS), and $Cu_{16}Bi_{16}Se_{32}$(CBS) with the $L1_1$ (AF-II) and $D4$ (AF-IIb) structure.

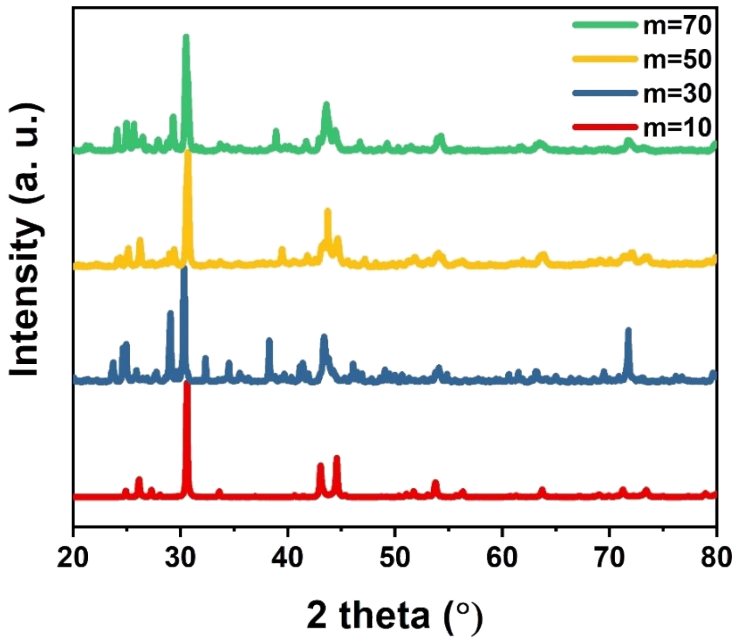

Figure S14. Room-temperature powder X-ray diffraction (PXRD) pattern of CABS-m (m=10, 30, 50, and 70). No single phase is obtained after m=30 in the process condition of this work.

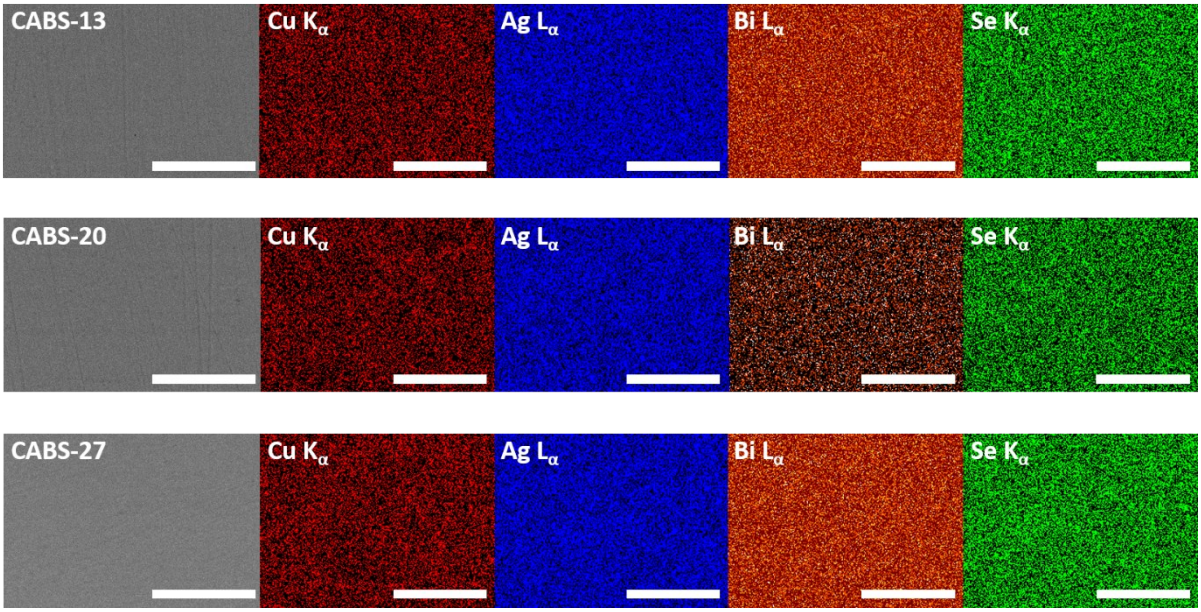

Figure S15. BSE-SEM images of polished surface of CABS-m with EDX elemental mapping, showing homogeneous distribution of elements within the sample. Scale bar = 50 μm.

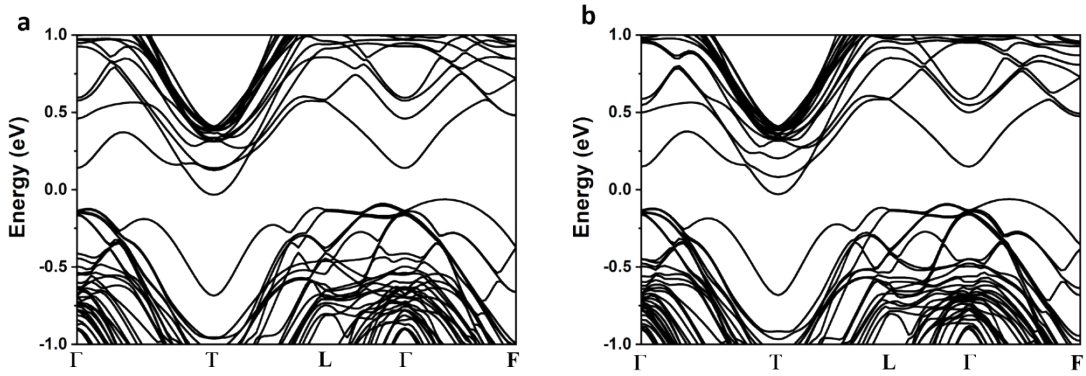

Figure S16. Calculated electronic band structure of $Cu_2Ag_{14}Bi_{16}Se_{32}$ with the $L1_1$ structure for different Cu-Cu distances. Both (a) the farthest configuration and (b) the nearest configuration shows a nestification of the conduction band at the T point. Spin-orbit interaction was included in the calculation.

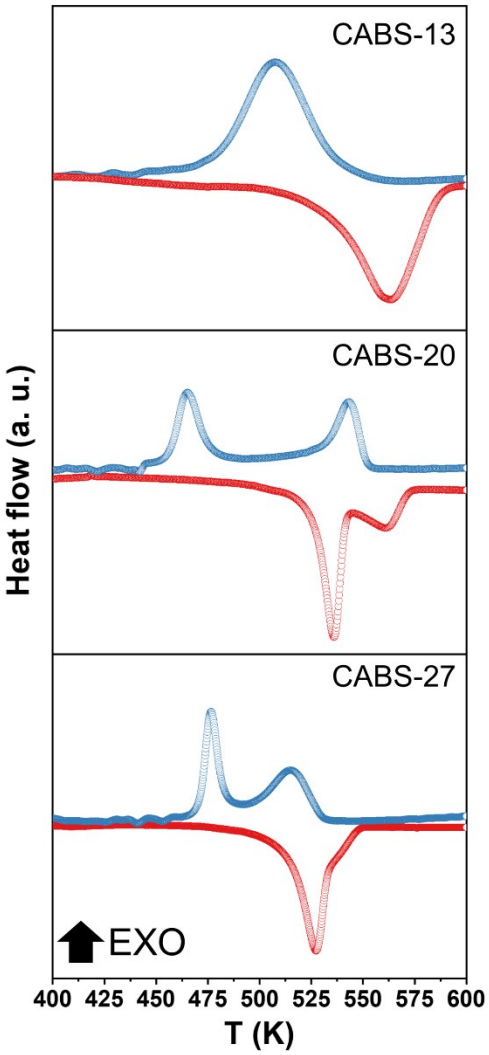

Figure S17. DSC experiment result of CABS alloys from 400 K to 600 K. A shift of the onset temperature of the phase transition is observed.

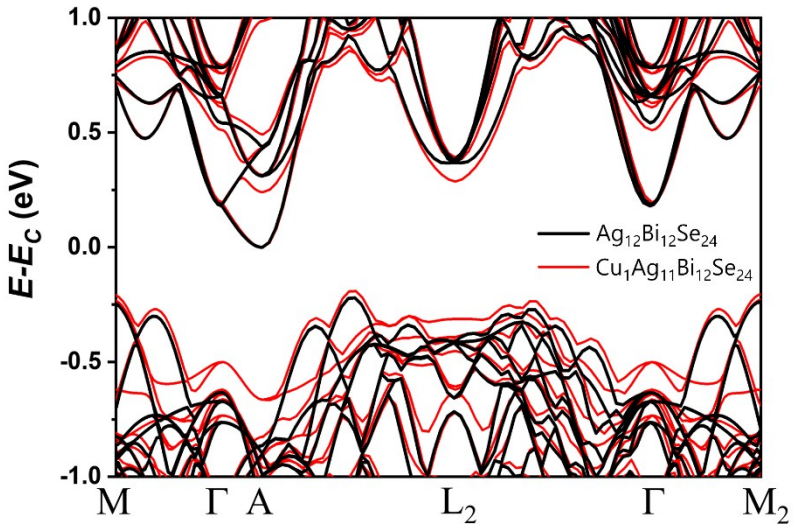

Figure S18. Calculated electronic structure of $Ag_{12}Bi_{12}Se_{24}$ and $Cu_1Ag_{11}Bi_{12}Se_{24}$ with the hexagonal structure. Spin-orbit interaction was not included in the calculation.

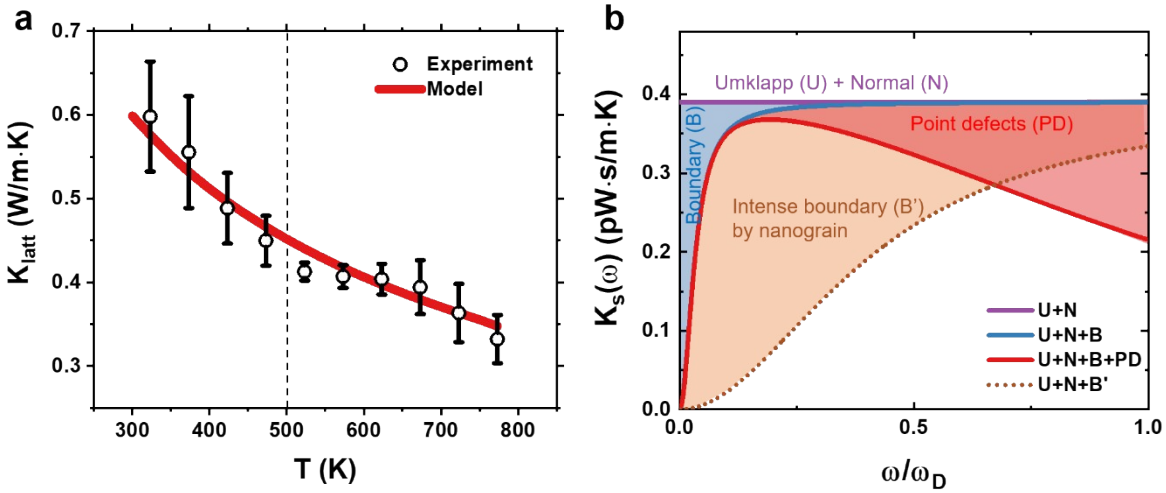

Figure S19. (a) The experimental lattice thermal conductivity of CABS-27 and (b) the spectral lattice thermal conductivity at 323 K. The phonon frequency was defined to the Debye frequency of ABS. Various scattering processes including Umklapp (U), normal (N), grain boundary of CABS-27 (B), and that of CABS-13 (B'), and point defects (PD) were considered.

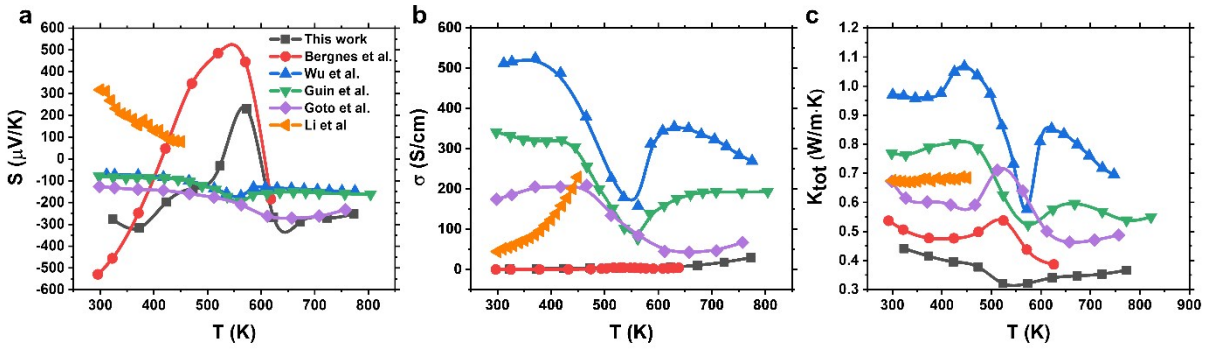

Figure S20. Temperature-dependent (a) Seebeck coefficient, (b) electrical conductivity, and (c) total thermal conductivity of $AgBiSe_2$. Reported TE properties of the pure $AgBiSe_2$ is plotted together for the comparison.

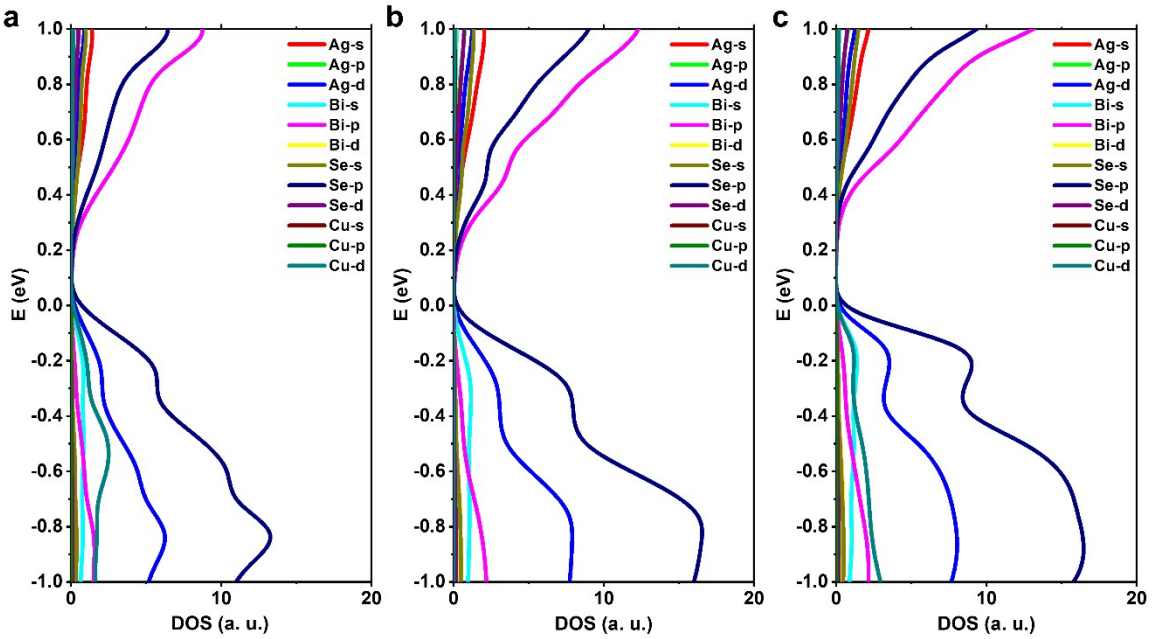

Figure S21. Atom-projected density of states of $Cu_1Ag_{15}Bi_{16}Se_{32}$ with the (a) hexagonal, (b) $L1_1$, and (c) $D4$ structure. Spin-orbit interaction was included in the calculation.

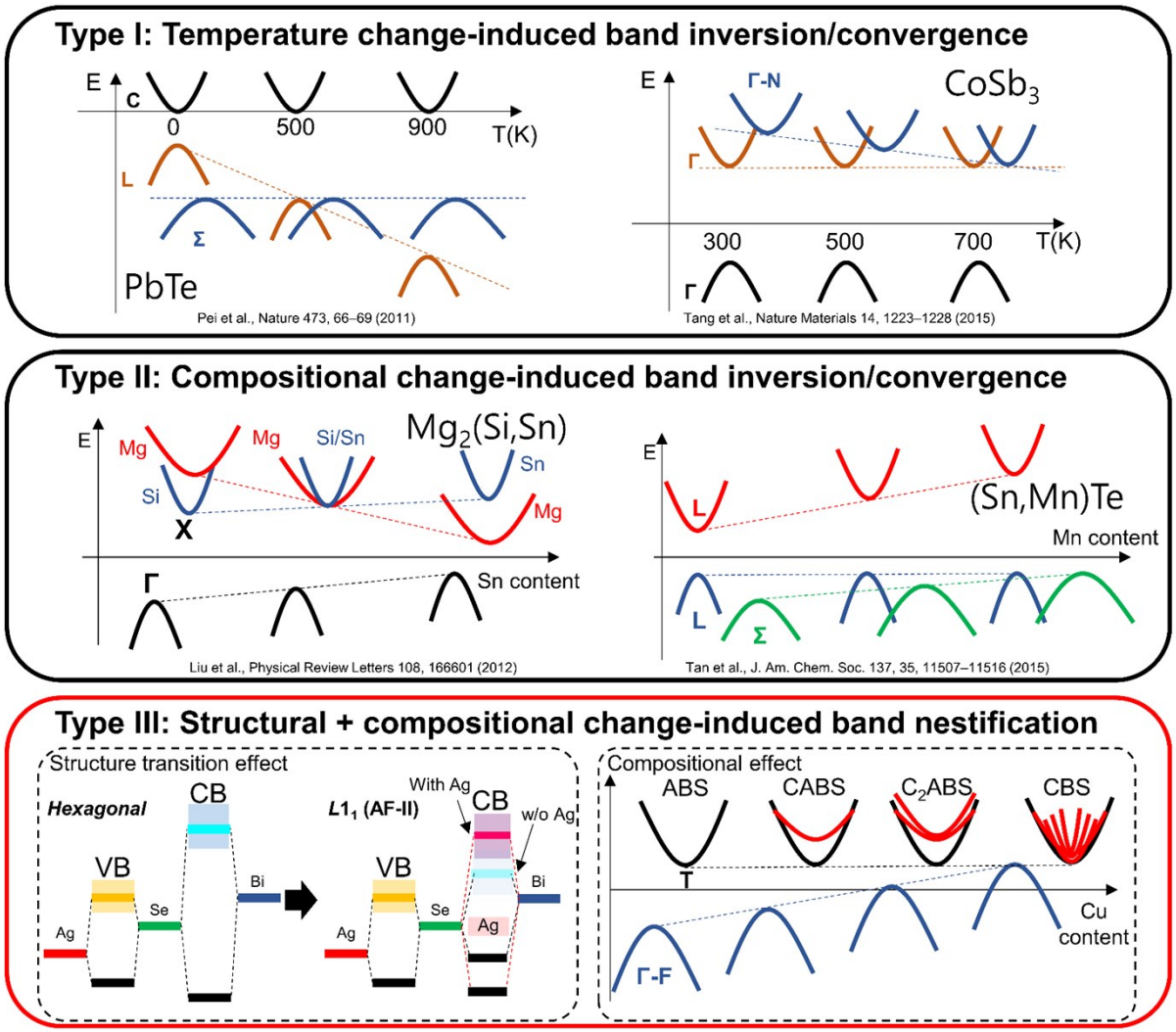

Figure S22. Comparison of previously reported mechanism of the band convergence (Type I, II) and the band nestification of this work (Type III).

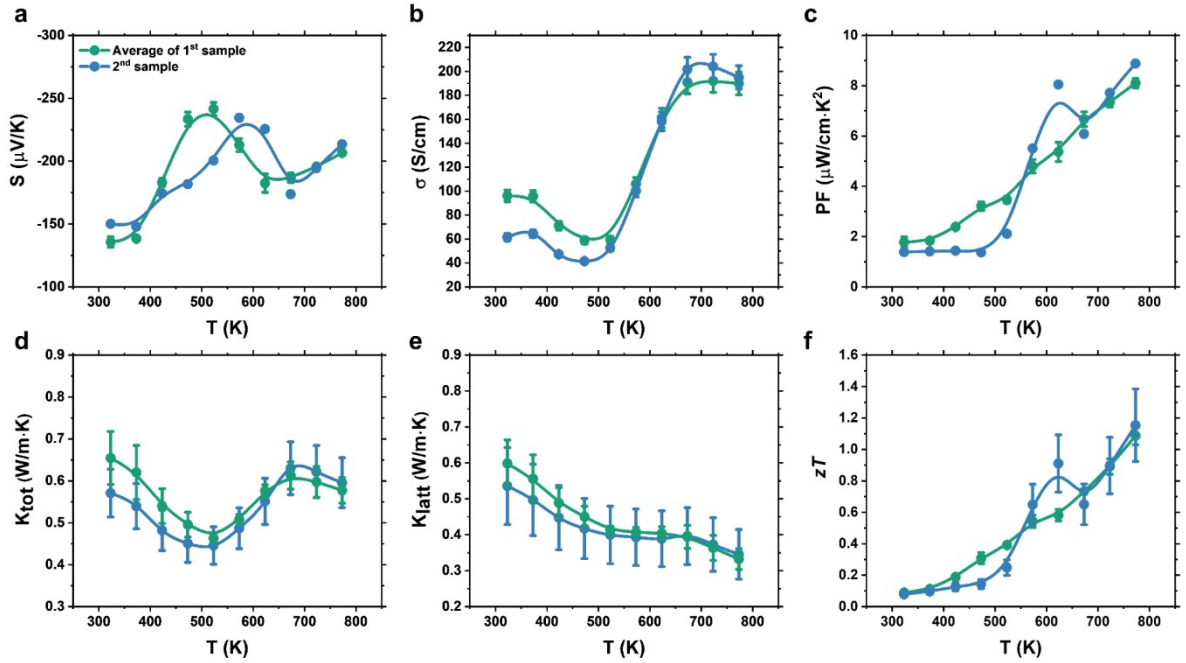

Figure S23. The temperature-dependent (a) Seebeck coefficient, (b) electrical conductivity, (c) power factor, (d) total thermal conductivity, (e) lattice thermal conductivity, and (f) zT values of independently prepared CABS-27. Each individual sample exhibits similar temperature dependence, especially at high temperatures.

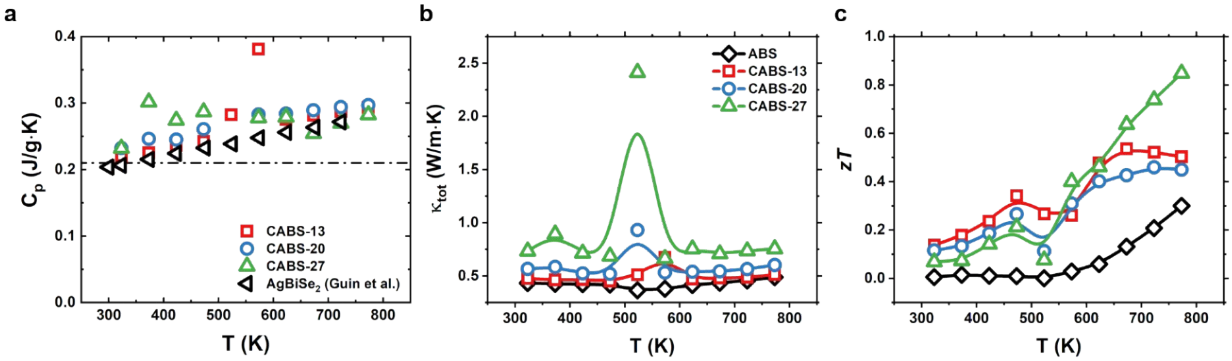

Figure S24. Temperature-dependent (a) specific heat capacity, (b) total thermal conductivity from measured C_p, and (c) corresponding zT values of CABS alloys.

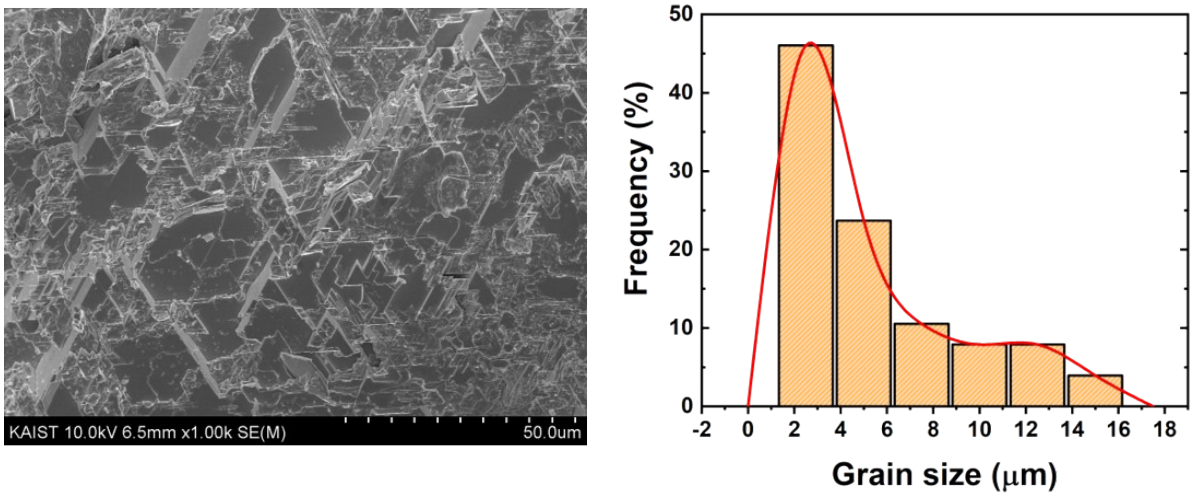

Figure S25. Low-magnification SEM image of the fracture surface of CABS-27 and its bimodal distribution of the grain size.

Atom	x	y	z	Atom	x	y	z
Ag1	0	0	0	Se1	0.245525	0.245525	0.254475
Ag2	0	0.25	0.25	Se2	0.245525	0.995525	0.004475
Ag3	0.25	0	0.25	Se3	0.995525	0.245525	0.004475
Ag4	0.25	0.25	0.5	Se4	0.004475	0.004475	0.245525
Ag5	0.25	0.75	0	Se5	0.254475	0.254475	0.745525
Ag6	0	0.5	0.5	Se6	0.254475	0.004475	0.495525
Ag7	0	0.75	0.75	Se7	0.004475	0.254475	0.495525
Ag8	0.25	0.5	0.75	Se8	0.995525	0.995525	0.754475
Ag9	0.75	0.25	0	Se9	0.254475	0.754475	0.245525
Ag10	0.5	0	0.5	Se10	0.254475	0.504475	0.995525
Ag11	0.5	0.25	0.75	Se11	0.004475	0.754475	0.995525
Ag12	0.75	0	0.75	Se12	0.995525	0.495525	0.254475
Ag13	0.5	0.5	0	Se13	0.245525	0.745525	0.754475
Ag14	0.5	0.75	0.25	Se14	0.245525	0.495525	0.504475
Ag15	0.75	0.5	0.25	Se15	0.995525	0.745525	0.504475
Ag16	0.75	0.75	0.5	Se16	0.004475	0.504475	0.745525
Bi1	0.25	0.25	0	Se17	0.754475	0.254475	0.245525
Bi2	0	0	0.5	Se18	0.754475	0.004475	0.995525
Bi3	0	0.25	0.75	Se19	0.504475	0.254475	0.995525
Bi4	0.25	0	0.75	Se20	0.495525	0.995525	0.254475
Bi5	0	0.5	0	Se21	0.745525	0.245525	0.754475
Bi6	0	0.75	0.25	Se22	0.745525	0.995525	0.504475
Bi7	0.25	0.5	0.25	Se23	0.495525	0.245525	0.504475
Bi8	0.25	0.75	0.5	Se24	0.504475	0.004475	0.745525
Bi9	0.5	0	0	Se25	0.745525	0.745525	0.254475
Bi10	0.5	0.25	0.25	Se26	0.745525	0.495525	0.004475
Bi11	0.75	0	0.25	Se27	0.495525	0.745525	0.004475
Bi12	0.75	0.25	0.5	Se28	0.504475	0.504475	0.245525
Bi13	0.75	0.75	0	Se29	0.754475	0.754475	0.745525
Bi14	0.5	0.5	0.5	Se30	0.754475	0.504475	0.495525
Bi15	0.5	0.75	0.75	Se31	0.504475	0.754475	0.495525
Bi16	0.75	0.5	0.75	Se32	0.495525	0.495525	0.754475

Table S1. Relaxed atomic position of the $Ag_{16}Bi_{16}Se_{32}$ (ABS) supercell with AF-II ($L1_1$) structure.

Atom	x	y	z	Atom	x	y	z
Ag1	0	0	0	Se1	0.254102	0.245898	0.254102
Ag2	0.25	0	0.25	Se2	0.245898	0.995898	0.004102
Ag3	0	0.25	0.75	Se3	0.995898	0.245898	0.995898
Ag4	0.25	0.25	0.5	Se4	0.004102	0.995898	0.245898
Ag5	0	0.75	0.25	Se5	0.245898	0.254102	0.745898
Ag6	0.25	0.75	0	Se6	0.254102	0.004102	0.495898
Ag7	0	0.5	0.5	Se7	0.004102	0.254102	0.504102
Ag8	0.25	0.5	0.75	Se8	0.995898	0.004102	0.754102
Ag9	0.5	0.25	0.25	Se9	0.245898	0.754102	0.245898
Ag10	0.75	0.25	0	Se10	0.254102	0.504102	0.995898
Ag11	0.5	0	0.5	Se11	0.004102	0.754102	0.004102
Ag12	0.75	0	0.75	Se12	0.995898	0.504102	0.254102
Ag13	0.5	0.5	0	Se13	0.254102	0.745898	0.754102
Ag14	0.75	0.5	0.25	Se14	0.245898	0.495898	0.504102
Ag15	0.5	0.75	0.75	Se15	0.995898	0.745898	0.495898
Ag16	0.75	0.75	0.5	Se16	0.004102	0.495898	0.745898
Bi1	0	0.25	0.25	Se17	0.745898	0.254102	0.245898
Bi2	0.25	0.25	0	Se18	0.754102	0.004102	0.995898
Bi3	0	0	0.5	Se19	0.504102	0.254102	0.004102
Bi4	0.25	0	0.75	Se20	0.495898	0.004102	0.254102
Bi5	0	0.5	0	Se21	0.754102	0.245898	0.754102
Bi6	0.25	0.5	0.25	Se22	0.745898	0.995898	0.504102
Bi7	0	0.75	0.75	Se23	0.495898	0.245898	0.495898
Bi8	0.25	0.75	0.5	Se24	0.504102	0.995898	0.745898
Bi9	0.5	0	0	Se25	0.754102	0.745898	0.254102
Bi10	0.75	0	0.25	Se26	0.745898	0.495898	0.004102
Bi11	0.5	0.25	0.75	Se27	0.495898	0.745898	0.995898
Bi12	0.75	0.25	0.5	Se28	0.504102	0.495898	0.245898
Bi13	0.5	0.75	0.25	Se29	0.745898	0.754102	0.745898
Bi14	0.75	0.75	0	Se30	0.754102	0.504102	0.495898
Bi15	0.5	0.5	0.5	Se31	0.504102	0.754102	0.504102
Bi16	0.75	0.5	0.75	Se32	0.495898	0.504102	0.754102

Table S2. Relaxed atomic position of the $Ag_{16}Bi_{16}Se_{32}$ (ABS) supercell with AF-IIb (*D*4) structure.

Atom	x	y	z	Atom	x	y	z
Ag1	0	0.249803402	0.249803402	Se1	0.245170298	0.245170298	0.254814502
Ag2	0.249803402	0	0.249803402	Se2	0.237280634	0.995453436	0.004546564
Ag3	0.249997538	0.249997538	0.500015515	Se3	0.995453436	0.237280634	0.004546564
Ag4	0.249803402	0.750196598	0	Se4	0.004546564	0.004546564	0.237280634
Ag5	0	0.5	0.5	Se5	0.254854092	0.254854092	0.745145908
Ag6	0	0.750196598	0.750196598	Se6	0.25450097	0.004789187	0.495144041
Ag7	0.249997538	0.499984485	0.750002462	Se7	0.004789187	0.25450097	0.495144041
Ag8	0.750196598	0.249803402	0	Se8	0.995453436	0.995453436	0.762719366
Ag9	0.5	0	0.5	Se9	0.254814502	0.754829702	0.245170298
Ag10	0.499984485	0.249997538	0.750002462	Se10	0.25450097	0.504855959	0.995210813
Ag11	0.750196598	0	0.750196598	Se11	0.004546564	0.762719366	0.995453436
Ag12	0.5	0.5	0	Se12	0.995210813	0.495144041	0.25450097
Ag13	0.500015515	0.750002462	0.249997538	Se13	0.245170298	0.745185498	0.754829702
Ag14	0.750002462	0.500015515	0.249997538	Se14	0.245163286	0.495204149	0.504795851
Ag15	0.750002462	0.750002462	0.499984485	Se15	0.995210813	0.74549903	0.504855959
Cu1	0	0	0	Se16	0.004789187	0.504855959	0.74549903
Bi1	0.24933419	0.24933419	-4.9023E-07	Se17	0.754829702	0.254814502	0.245170298
Bi2	0	0	0.5	Se18	0.762719366	0.004546564	0.995453436
Bi3	4.9023E-07	0.24933419	0.75066581	Se19	0.504855959	0.25450097	0.995210813
Bi4	0.24933419	4.9023E-07	0.75066581	Se20	0.495144041	0.995210813	0.25450097
Bi5	0	0.5	0	Se21	0.745185498	0.245170298	0.754829702
Bi6	-4.9023E-07	0.75066581	0.24933419	Se22	0.74549903	0.995210813	0.504855959
Bi7	0.249977315	0.5	0.249977315	Se23	0.495204149	0.245163286	0.504795851
Bi8	0.249977315	0.750022685	0.5	Se24	0.504855959	0.004789187	0.74549903
Bi9	0.5	0	0	Se25	0.745145908	0.745145908	0.254854092
Bi10	0.5	0.249977315	0.249977315	Se26	0.74549903	0.495144041	0.004789187
Bi11	0.75066581	-4.9023E-07	0.24933419	Se27	0.495144041	0.74549903	0.004789187
Bi12	0.750022685	0.249977315	0.5	Se28	0.504795851	0.504795851	0.245163286
Bi13	0.75066581	0.75066581	4.9023E-07	Se29	0.754829702	0.754829702	0.745185498
Bi14	0.5	0.5	0.5	Se30	0.754836714	0.504795851	0.495204149
Bi15	0.5	0.750022685	0.750022685	Se31	0.504795851	0.754836714	0.495204149
Bi16	0.750022685	0.5	0.750022685	Se32	0.495204149	0.495204149	0.754836714

Table S3. Relaxed atomic position of the $Cu_1Ag_{15}Bi_{16}Se_{32}$ (CABS) supercell with AF-II ($L1_1$) structure.

Atom	x	y	z	Atom	x	y	z
Ag1	0.249757	2.34E-06	0.249757	Se1	0.254379	0.245589	0.254379
Ag2	2.34E-06	0.249757	0.750243	Se2	0.23776	0.995869	0.004131
Ag3	0.249999	0.249999	0.5	Se3	0.995869	0.23776	0.995869
Ag4	-2.3E-06	0.750243	0.249757	Se4	0.004131	0.995869	0.23776
Ag5	0.249757	0.750243	-2.3E-06	Se5	0.245589	0.254379	0.745621
Ag6	0	0.5	0.5	Se6	0.254003	0.004343	0.495565
Ag7	0.249999	0.5	0.750001	Se7	0.004343	0.254003	0.504435
Ag8	0.5	0.249999	0.249999	Se8	0.995869	0.004131	0.76224
Ag9	0.750243	0.249757	2.34E-06	Se9	0.245653	0.754347	0.245653
Ag10	0.5	0	0.5	Se10	0.254003	0.504435	0.995657
Ag11	0.750243	-2.3E-06	0.750243	Se11	0.004131	0.76224	0.004131
Ag12	0.5	0.5	0	Se12	0.995657	0.504435	0.254003
Ag13	0.750001	0.5	0.249999	Se13	0.254379	0.745621	0.754411
Ag14	0.5	0.750001	0.750001	Se14	0.245606	0.495644	0.504356
Ag15	0.750001	0.750001	0.5	Se15	0.995657	0.745997	0.495565
Cu1	0	0	0	Se16	0.004343	0.495565	0.745997
Bi1	0	0.24927	0.24927	Se17	0.745621	0.254379	0.245589
Bi2	0.24927	0.24927	0	Se18	0.76224	0.004131	0.995869
Bi3	0	0	0.5	Se19	0.504435	0.254003	0.004343
Bi4	0.24927	0	0.75073	Se20	0.495565	0.004343	0.254003
Bi5	0	0.5	0	Se21	0.754347	0.245653	0.754347
Bi6	0.249975	0.499988	0.249975	Se22	0.745997	0.995657	0.504435
Bi7	0	0.75073	0.75073	Se23	0.495644	0.245606	0.495644
Bi8	0.249975	0.750025	0.500012	Se24	0.504435	0.995657	0.745997
Bi9	0.5	0	0	Se25	0.754411	0.745621	0.254379
Bi10	0.75073	0	0.24927	Se26	0.745997	0.495565	0.004343
Bi11	0.499988	0.249975	0.750025	Se27	0.495565	0.745997	0.995657
Bi12	0.750025	0.249975	0.499988	Se28	0.504356	0.495644	0.245606
Bi13	0.500012	0.750025	0.249975	Se29	0.745621	0.754411	0.745621
Bi14	0.75073	0.75073	0	Se30	0.754394	0.504356	0.495644
Bi15	0.5	0.5	0.5	Se31	0.504356	0.754394	0.504356
Bi16	0.750025	0.500012	0.750025	Se32	0.495644	0.504356	0.754394

Table S4. Relaxed atomic position of the $Cu_1Ag_{15}Bi_{16}Se_{32}$ (CABS) supercell with AF-IIb (*D*4) structure.

Atom	x	y	z	Atom	x	y	z
Cu1	0	0	0	Se1	0.237231	0.237231	0.262769
Cu2	0	0.25	0.25	Se2	0.237231	0.987231	0.012769
Cu3	0.25	0	0.25	Se3	0.987231	0.237231	0.012769
Cu4	0.25	0.25	0.5	Se4	0.012769	0.012769	0.237231
Cu5	0.25	0.75	0	Se5	0.262769	0.262769	0.737231
Cu6	0	0.5	0.5	Se6	0.262769	0.012769	0.487231
Cu7	0	0.75	0.75	Se7	0.012769	0.262769	0.487231
Cu8	0.25	0.5	0.75	Se8	0.987231	0.987231	0.762769
Cu9	0.75	0.25	0	Se9	0.262769	0.762769	0.237231
Cu10	0.5	0	0.5	Se10	0.262769	0.512769	0.987231
Cu11	0.5	0.25	0.75	Se11	0.012769	0.762769	0.987231
Cu12	0.75	0	0.75	Se12	0.987231	0.487231	0.262769
Cu13	0.5	0.5	0	Se13	0.237231	0.737231	0.762769
Cu14	0.5	0.75	0.25	Se14	0.237231	0.487231	0.512769
Cu15	0.75	0.5	0.25	Se15	0.987231	0.737231	0.512769
Cu16	0.75	0.75	0.5	Se16	0.012769	0.512769	0.737231
Bi1	0.25	0.25	0	Se17	0.762769	0.262769	0.237231
Bi2	0	0	0.5	Se18	0.762769	0.012769	0.987231
Bi3	0	0.25	0.75	Se19	0.512769	0.262769	0.987231
Bi4	0.25	0	0.75	Se20	0.487231	0.987231	0.262769
Bi5	0	0.5	0	Se21	0.737231	0.237231	0.762769
Bi6	0	0.75	0.25	Se22	0.737231	0.987231	0.512769
Bi7	0.25	0.5	0.25	Se23	0.487231	0.237231	0.512769
Bi8	0.25	0.75	0.5	Se24	0.512769	0.012769	0.737231
Bi9	0.5	0	0	Se25	0.737231	0.737231	0.262769
Bi10	0.5	0.25	0.25	Se26	0.737231	0.487231	0.012769
Bi11	0.75	0	0.25	Se27	0.487231	0.737231	0.012769
Bi12	0.75	0.25	0.5	Se28	0.512769	0.512769	0.237231
Bi13	0.75	0.75	0	Se29	0.762769	0.762769	0.737231
Bi14	0.5	0.5	0.5	Se30	0.762769	0.512769	0.487231
Bi15	0.5	0.75	0.75	Se31	0.512769	0.762769	0.487231
Bi16	0.75	0.5	0.75	Se32	0.487231	0.487231	0.762769

Table S5. Relaxed atomic position of the $Cu_{16}Bi_{16}Se_{32}$ (CBS) supercell with AF-II ($L1_1$) structure.

Atom	x	y	z	Atom	x	y	z
Cu1	0	0	0	Se1	0.26296	0.23704	0.26296
Cu2	0.25	0	0.25	Se2	0.23704	0.98704	0.01296
Cu3	0	0.25	0.75	Se3	0.98704	0.23704	0.98704
Cu4	0.25	0.25	0.5	Se4	0.01296	0.98704	0.23704
Cu5	0	0.75	0.25	Se5	0.23704	0.26296	0.73704
Cu6	0.25	0.75	0	Se6	0.26296	0.01296	0.48704
Cu7	0	0.5	0.5	Se7	0.01296	0.26296	0.51296
Cu8	0.25	0.5	0.75	Se8	0.98704	0.01296	0.76296
Cu9	0.5	0.25	0.25	Se9	0.23704	0.76296	0.23704
Cu10	0.75	0.25	0	Se10	0.26296	0.51296	0.98704
Cu11	0.5	0	0.5	Se11	0.01296	0.76296	0.01296
Cu12	0.75	0	0.75	Se12	0.98704	0.51296	0.26296
Cu13	0.5	0.5	0	Se13	0.26296	0.73704	0.76296
Cu14	0.75	0.5	0.25	Se14	0.23704	0.48704	0.51296
Cu15	0.5	0.75	0.75	Se15	0.98704	0.73704	0.48704
Cu16	0.75	0.75	0.5	Se16	0.01296	0.48704	0.73704
Bi1	0	0.25	0.25	Se17	0.73704	0.26296	0.23704
Bi2	0.25	0.25	0	Se18	0.76296	0.01296	0.98704
Bi3	0	0	0.5	Se19	0.51296	0.26296	0.01296
Bi4	0.25	0	0.75	Se20	0.48704	0.01296	0.26296
Bi5	0	0.5	0	Se21	0.76296	0.23704	0.76296
Bi6	0.25	0.5	0.25	Se22	0.73704	0.98704	0.51296
Bi7	0	0.75	0.75	Se23	0.48704	0.23704	0.48704
Bi8	0.25	0.75	0.5	Se24	0.51296	0.98704	0.73704
Bi9	0.5	0	0	Se25	0.76296	0.73704	0.26296
Bi10	0.75	0	0.25	Se26	0.73704	0.48704	0.01296
Bi11	0.5	0.25	0.75	Se27	0.48704	0.73704	0.98704
Bi12	0.75	0.25	0.5	Se28	0.51296	0.48704	0.23704
Bi13	0.5	0.75	0.25	Se29	0.73704	0.76296	0.73704
Bi14	0.75	0.75	0	Se30	0.76296	0.51296	0.48704
Bi15	0.5	0.5	0.5	Se31	0.51296	0.76296	0.51296
Bi16	0.75	0.5	0.75	Se32	0.48704	0.51296	0.76296

Table S6. Relaxed atomic position of the $Cu_{16}Bi_{16}Se_{32}$ (CBS) supercell with AF-IIb (*D*4) structure.

Relationship between the phase transition and Cu content in CABS alloys

As observed in the transport properties, Cu content significantly affects the transition temperature of CABS alloys. Hence, to study on the phase transition behavior, we conducted DSC experiment for CABS alloys (Figure S17). The main observation is that the onset transition temperature from rhombohedral to cubic phase linearly decreases with following relationship:

$$T_{R\rightarrow C} = 533.9 - 0.7429 * m\ (K)$$

where m denotes the atomic percent of Cu substituting Ag sites. Similar observations were made to other ABS-related materials when an isovalent element was alloyed in the matrix, while its physical origin is not fully understood (Goto et al., Dalton Trans., 2018,47, 2575-2580; Bernges et al., Inorg. Chem. 2019, 58, 14, 9236–9245; Mitra et al., Cryst. Res. Technol. 52, No. 6, 1700075 (2017)).

Interestingly, the transition peak splits into two in CABS-20 with one peak at lower temperature, and CABS-27 has a broad shoulder in its peak**. This result should be mainly attributed to the effect of the grain size of CABS alloys**. It was reported that a material with small grains tends to have a broad transition peak when it experiences the phase transition (Mao et al., Journal of the European Ceramic Society 34, 2933–2939 (2014)). Also, in organic-inorganic halide perovskite, the suppression of the phase transition in small grain samples occurs, shifting the phase transition temperature to higher value (Stavrakas et al., Adv. Energy Mater. 2019, 9, 1901883). The main reason for the broad and suppressed phase transition is that **small grains are not capable of rearrange their crystal structure as easily as large grains** due to mechanical constrain effect of grain boundaries.

As observed in the SEM image of the fracture surface of CABS-13 (Figure S2), the average grain size is approximately 200 nm, while CABS-27 has the average grain size of approximately 15 μm. Therefore, as Cu concentration increases, the constrain effect of the grain would be smaller, making grains easier to experience the phase transition at lower temperature. Based on above discussion, our conclusion on DSC experiment is as follows:

i) The broad and uniform transition peak at the high temperature is due to a narrow grain size distribution of CABS-13 with small grain sizes

ii) Between two transition peaks of CABS-20, the transition peak emerges at lower temperature because large grains in the sample experiences weaker constrain effect. The second transition peak shows similar transition temperature, implying that nano-grains still exist in the sample.

iii) The major transition peak is merged with a minor peak originating from the small grain. Because of the increase of the average grain size, small grains are not small as that of CABS-13 or CABS-20. Therefore, the transition temperature is similar to that of large grains, remaining a large shoulder due to the broadness of the peak.

Calculation of the theoretical lattice thermal conductivity

We calculated the theoretical lattice thermal conductivity by

$$\kappa_{latt} = \frac{k_B}{2\pi^2 \upsilon}\left(\frac{k_B T}{\hbar}\right)^3 \int_0^{\frac{\theta_D}{T}} \tau(z) \frac{z^4 exp(z)}{[\exp(z)-1]^2} dz$$

where υ is the average sound velocity and θ_D is Debye temperature of $AgBiSe_2$. For determination of relaxation time, Umklapp process, normal process, grain boundary, and point defects are considered in the calculation. The relaxation time of each process is given as follows:

$$\tau_U^{-1} + \tau_N^{-1} = \beta \frac{2}{(6\pi^2)^{1/3}} \frac{k_B \bar{V}^{1/3} \gamma^2 \omega^2 T}{\bar{M} \upsilon^3} \quad \text{(Umklapp and normal process)}$$

$$\tau_{PD}^{-1} = \frac{\bar{V}\omega^4}{4\pi \upsilon^3} \Gamma \quad \text{(Point defects)}$$

$$\tau_B^{-1} = \frac{\upsilon}{d} \quad \text{(Grain boundary)}$$

The total relaxation time is given by Matthiessen's rule as: $\tau^{-1} = \tau_U^{-1} + \tau_N^{-1} + \tau_B^{-1} + \tau_{PD}^{-1}$. Elastic properties were adopted from the work of Böcher et al. (Dalton Trans., 2017,46, 3906-3914). The scattering parameter for point defect (Γ) is calculated according to the previously reported method (Koh et al., Applied Physics Letters 94, 153101). The model predicts the experimental lattice thermal conductivity well with negligible deviation. A small difference between the model and the experiment is due to additional scattering during the phase transition, which causes critical scattering and phase boundary scattering.

To better understand the effect of each scattering process on phonon transport, we also estimated the spectral lattice thermal conductivity as a function of phonon frequency. one can easily notice that the boundary scattering (B) of CABS-27 is only limited to the low-frequency phonon due to large average grain size. In CABS-27, it is the point defects scattering which effectively suppresses high frequency phonons. However, if we decrease the size of grain to ~200 nm, which is the average grain size of CABS-13, the boundary scattering of CABS-13 (B') can scatter phonons having frequency from zero to Debye frequency. This calculation result demonstrates that **the rise of the lattice thermal conductivity near room temperature is reasonable, considering a significant larger grain size of CABS-27 than that of CABS-13**.

Symbols	Description	Value
β	Integrating factor of Umklapp and Normal process	2.3
$\bar{V}$	Average atomic volume of $AgBiSe_2$	2.97×10^{-28} m^3
$\bar{M}$	Average atomic mass of $AgBiSe_2$	7.88×10^{-25} kg
υ	Average sound velocity	1358 m/s
γ	Grüneisen parameter	1.6
r	Poisson's ratio	0.265
θ_D	Debye temperature	138 K

Table S7. Parameters used to calculate the theoretical lattice thermal conductivity of CABS alloys.

Calculation of electronic transport properties with the three-band model

To evaluate the effect of band convergence on the thermoelectric properties, electronic transport properties were calculated based on the three-band model, which is described by light conduction band (L band, C_L), heavy conduction band (H band, C_H), and valence band (V band, V). The relationship between the reduced Fermi energy of band is given by the following equation:

$$\eta_H = \eta_L - \frac{\Delta}{k_B T} \tag{1}$$

$$\eta_V = -\frac{E_g}{k_B T} - \eta_L \tag{2}$$

where η_L, η_H, η_V are the reduced Fermi energy of the light conduction band, heavy conduction band, and the valence band, respectively. Δ is the energy offset between L band and H band, and E_g is the band gap between L band and V band.

The temperature dependence of Δ and E_g is estimated by following equation:

$$\frac{d\Delta}{dT} = a_1 \times 10^{-4}\, eV/K \tag{3}$$

$$\frac{dE_g}{dT} = a_2 \times 10^{-4}\, eV/K \tag{4}$$

where a_1 and a_2 is a fitting parameter for the energy offset and band gap, respectively.

From Fermi-Dirac statistics, carrier concentration of each band is given by following equation:

$$n_{C_L} = 2\left(\frac{2\pi m_{C_L}^* k_B T}{h^2}\right)^{\frac{3}{2}} F_{1/2}(\eta_{C_L}) \tag{5}$$

$$n_{C_H} = 2\left(\frac{2\pi m_{C_H}^* k_B T}{h^2}\right)^{\frac{3}{2}} F_{1/2}(\eta_{C_H}) \tag{6}$$

$$p_V = 2\left(\frac{2\pi m_V^* k_B T}{h^2}\right)^{\frac{3}{2}} F_{1/2}(\eta_V) \tag{7}$$

where n_{C_L}, n_{C_H}, and p_V, and $m_{C_L}^*$, $m_{C_H}^*$, and m_V^* are the carrier concentration and density-of-states effective mass of L band, H band, and V band, respectively. k_B is Boltzmann constant, and h is Planck constant. Fermi-Dirac integral with order of *i* is defined as follow.

$$F_i(\eta) = \int_0^\infty \frac{u^i}{1 + exp(u - \eta)} du \tag{8}$$

Hence, total carrier concentration is the sum of n_{C_L}, n_{C_H}, and p_V.

To calculate the mobility of charge carriers, deformation potential scattering (acoustic phonon scattering) and

alloy scattering were considered. The carrier mobility for deformation potential scattering is expressed as follow:

$$\mu_{e-ph} = \frac{\sqrt{2}\pi e\hbar^4 \quad v^2\rho \quad F_0(\eta)}{3(k_BT)^{3/2}(E_{def})^2(m_b^*)^{5/2}F_{1/2}(\eta)} \tag{9}$$

where m_b^* is the band effective mass, E_{def} is deformation potential, v is the longitudinal sound velocity, ρ is the bulk density, $\hbar$ is reduced Planck constant, and e is the elementary charge.

Similarly, the mobility of charge carriers by alloy scattering is given by following equation:

$$\mu_{alloy} = \frac{16e\hbar^4 \quad N_0 \quad F_0(\eta)}{9\sqrt{2}\pi x(1-x)(k_BT)^{1/2}U^2(m_b^*)^{5/2}F_{1/2}(\eta)} \tag{10}$$

where N_0 is the number density of the atoms in the unit cell, x is the fractional occupation of the alloying element, and U is the alloy scattering potential. The total carrier mobility was calculated by Matthiessen's rule.

The Seebeck coefficient of each band for acoustic phonon scattering is given by following equation:

$$S_{C_L}(\eta_{C_L}) = -\frac{e}{k_B}\left(\frac{F_1(\eta_{C_L})}{F_0(\eta_{C_L})} - \eta_{C_L}\right) \tag{11}$$

$$S_{C_H}(\eta_{C_H}) = -\frac{e}{k_B}\left(\frac{F_1(\eta_{C_H})}{F_0(\eta_{C_H})} - \eta_{C_H}\right) \tag{12}$$

$$S_V(\eta_V) = -\frac{e}{k_B}\left(\frac{F_1(\eta_V)}{F_0(\eta_V)} - \eta_V\right) \tag{13}$$

Total electrical conductivity and total Seebeck coefficient are given by following equation:

$$\sigma_{tot} = \sigma_{C_L} + \sigma_{C_H} + \sigma_V \tag{14}$$

$$S_{tot} = \frac{S_{C_L}\sigma_{C_L} + S_{C_H}\sigma_{C_H} + S_V\sigma_V}{\sigma_{tot}} \tag{15}$$

Table below summarizes material parameters used to calculate PF by the three-band model. Note that other sets of parameters may exist which give better fittings to the experimental values.

Symbols	Description	Value
$m_{C_L}^*$	L band effective mass	0.4 m_0
$m_{C_H}^*$	H band effective mass	12.0 m_0
m_V^*	V band effective mass	3.0 m_0
Δ	Band offset between L band and H band.	0.176-0.00022T eV

E_g	Band gap between L band and V band.	0.588-0.00003T eV
E_{def}	Deformation potential of C band and L band	11.68 eV
U	Alloy scattering potential	2.0 eV
$\boldsymbol{v}$	Longitudinal sound velocity	3280 m/s
$\boldsymbol{N_{V,L}}$	Valley degeneracy of L band	3
$\boldsymbol{N_{V,H}}$	Valley degeneracy of H band	6
$\boldsymbol{N_{V,V}}$	Valley degeneracy of V band	3

Table S8. Material parameters used for the three-band model calculation.